35th AIAA Fluid Dynamics Conference and Exhibit
6-9 June 2005, Toronto, Ontario, Canada

AIAA Paper 2005-5022

EFFECT OF NOSE BLUNTNESS ON HYPERSONIC BOUNDARY LAYER RECEPTIVITY OVER A BLUNT CONE

Xiaolin Zhong *
University of California, Los Angeles, California 90095

A numerical simulation study is conducted on the effect of nose bluntness on the receptivity to weak free-stream fast acoustic waves for a Mach 7.99 axisymmetric flow over a 7° half-angle blunt cone. The flow conditions and geometry are the same as those used in Stetson's (1984) stability experiment. Three cases of different nose radii are considered covering both "small" and "large" nose bluntness in the context of the transition reversal phenomenon. A total of 15 frequencies are computed in the receptivity simulation for each case. It is found that the basic receptivity mechanism of hypersonic flow over the blunt cone with different nose radii is essentially the same. Specifically, the receptivity is a result of the resonant interactions between forcing waves and boundary-layer wave modes near the nose region, and the resonant interactions between different boundary-layer wave modes downstream. As the nose radius increases from "small" to "large", the current results show no reversal in the location of instability wave induced by the receptivity process. The location of initial excitation of the second instability mode always moves downstream as the nose bluntness is increased. In order to understand the cause of the transition reversal phenomenon, it is necessary to conduct further studies on the nose bluntness effects under other factors, which include receptivity to different forcing waves, surface roughness, larger nose bluntness, three-dimensional waves, and nonlinear interaction.

I. INTRODUCTION

The accurate prediction of laminar-turbulent transition in hypersonic boundary layers is a critical part of the aerodynamic heating analyses on hypersonic vehicles. Despite decades of extensive research, the prediction of hypersonic boundary-layer transition is still mostly based on empirical correlation methods or the semi-empirical e^n method because a number of physical mechanisms leading to transition are currently not well understood. The receptivity phenomenon, which is the process of environmental disturbances initially entering the boundary layers and generating disturbance waves, is one of these important, but less understood, mechanisms.

Stetson *et al.* (1984 & 1993) carried out boundary-layer stability experiments on an axisymmetric blunt cone in a Mach 7.99 free stream. The half angle of the cone was 7°, and the free-stream Reynolds number based on the nose radius was 33,449. The Reynolds number based on the total length of the cone is about 9 millions. Detailed fluctuation spectra of the disturbance waves developing along the body surface were measured in the experiments. It was found that the disturbances in the boundary layer were dominated by the second mode instability. Significant super harmonic components of the second modes were observed

*Professor, Mechanical and Aerospace Engineering Department, Associate Fellow AIAA. E-mail: xiaolin@ucla.edu.

after the second mode became dominant. Compared with similar hypersonic flow over a sharp cone, the second mode instability of the blunt cone appeared in much further downstream locations. This indicates a stabilization of the boundary layer by slight nose bluntness. Stability experiments of hypersonic flows over sharp or blunt cones have also been carried out by other researchers. Demetriades (1974 & 1977) did extensive stability experiments on hypersonic boundary layers over axisymmetric cones. Recently, Maslov and his colleagues (2001 & 2002) reported their stability experiments on supersonic and hypersonic flows over sharp or blunt cones.

The normal-mode linear stability characteristics of the boundary-layer flow over the same blunt cone as Stetson *et al.*'s experiments have been studied by a number of researchers (Malik *et al.* 1990, Herbert *et al.* 1993, Kufner *et al.* 1993 & 1994). Malik *et al.* (1990) computed the neutral stability curve and compared the growth rates obtained by LST with the experimental results. The steady base flow solution was computed by using the parabolized Navier-Stokes equations. They found that the nose bluntness stabilizes the boundary layer. The growth rates predicted by the LST were compared with Stetson *et al.*'s experimental results at the surface location of $s = 175$ nose radii ($0.667m$). The linear stability analyses predicted slightly lower frequency for the dominant second mode, but much higher amplification rates than the experimental results.

Rosenboom et al. (1999) did further study on the effect of nose bluntness on the linear stability of hypersonic flow over Stetson's blunt cone. In their studies, the cone geometry and freestream conditions were adapted to the Stetson's experiments. Three cases of blunt cones of different nose radii, which cover both "small" and "large" bluntness, were considered. The purpose was to investigate, by linear stability analysis, the transition reversal phenomenon observed in experiments at "large" bluntness (Potter and Whitfield 1962, Ericsson 1987). The transition reversal phenomenon refers to the experimental observation that the transition location moves downstream when the nose radius is increased. This trend is, however, reversed when the nose radius is larger than a certain critical value. Increasing nose radius after that will lead to a forward movement of the transition location. The downstream movement of the transition location at small radii can be explained by the reduction of local Reynolds numbers owing to the entropy layer created by the nose bluntness. However, there is still no satisfactory explanation for the cause of transition reversal at large nose bluntness. By a linear stability analysis, Rosenboom et al. (1999) confirmed a monotonic downstream movement of the second mode critical Reynolds number as nose radius increases. However, their linear stability analysis still cannot explain the transition reversal phenomena observed in experiment at "large" bluntness. Their results indicated that there is a need for better understanding of boundary layer receptivity as well as nonlinear transition phenomena for engineering transition predication.

This paper presents a numerical study on the effects of nose bluntness on the receptivity to free-stream acoustic waves for hypersonic flow by comparing the results of three nose radii. The flow conditions duplicate the experiments of Stetson *et al.* (1984) and aim to investigate the effects of nose bluntness on receptivity. The three nose radii are chosen to be the same as those used in Rosenboom et al.'s stability analysis. They are $3.81mm$ (Case A), $17.78mm$ (Case B), and $42.67mm$ (Case C). As stated by Rosenboom et al., the first nose radius belongs to category of "small" nose bluntness, while the second and third cases fall into the region of "large" bluntness. By using the numerical simulation, the initial receptivity process can be computed accurately in the current stury. The effects of bow shock interaction with forcing waves, the effects of the entropy layer and non-parallel boundary layer are also taken into account in the numerical simulation.

The current work is a continuation of a previous paper (Zhong and Ma 2003) regarding a numerical simulation study of the receptivity to weak free-stream fast acoustic waves corresponding to Stetson's experiments. In (Zhong and Ma 2003), the numerical results for the steady base flow were compared with the experimental results of Stetson *et al.* (1984), and with the numerical results of Esfahanian(1991). In addition, a normal-mode linear stability analysis was used to identify the main components of boundary-layer disturbances generated by forcing free-stream fast acoustic waves. It was found that neither the first mode nor the second-mode instability waves are excited directly by free-stream fast acoustic waves in the early region along the cone surface, although the Mack modes can be unstable there. Instead, the second mode is excited downstream of the second-mode Branch I neutral stability point. The delay of the second-mode excitation is a result of the fact that the hypersonic boundary-layer receptivity is governed by a two-step

resonant interaction process: 1) resonant interactions between the forcing waves and a stable boundary-layer wave mode I near the leading edge region, and 2) resonant interactions between the induced stable mode I and the unstable second Mack mode downstream. The nose radius was fixed at $3.81mm$ in (Zhong and Ma 2003). The effects of nose bluntness was not studies. This paper continues this study by investigating the nose bluntness effects.

II. GOVERNING EQUATIONS AND NUMERICAL METHODS

The governing equations for both steady and unsteady flow computations are briefly presented in this section. Details of the governing equations and numerical methods for two and three-dimensional flows have been described in previously papers (Zhong 1996 & 1996b). The governing equations are the unsteady three-dimensional Navier-Stokes equations written in the following conservation-law form:

$$\frac{\partial U^*}{\partial t^*} + \frac{\partial {F^*}_j}{\partial x_j^*} + \frac{\partial {F^*}_{vj}}{\partial x_j^*} = 0 \tag{1}$$

where $U^* = (\rho^*, \rho^* u_1^*, \rho^* u_2^*, \rho^* u_3^*, e^*)$, and superscript "$*$" represents dimensional variables. The Cartesian coordinates, $(x^*,\ y^*,\ z^*)$, are represented by $(x_1^*,\ x_2^*,\ x_3^*)$ in tensor notation. In the current simulation of axisymmetric flow over a blunt cone, x^* axis is along the center line of the axisymmetric cone pointing downstream. The origin of the Cartesian coordinate system is located at the center of the spherical nose.

We nondimensionalize the flow velocities by the free-stream velocity U_∞^*, length scales by the nose radius r_n^*, density by ρ_∞^*, pressure by p_∞^*, temperature by T_∞^*, time by r_n^*/U_∞^*, etc. The dimensionless flow variables are denoted by the same dimensional notation but without the superscript "$*$".

A fifth-order shock-fitting method of Zhong (1998) is used to compute the flow field bounded by the bow shock and wall surface, The flow variables behind the shock are determined by the Rankine-Hugoniot relations across the shock and a characteristic compatibility equation from behind the shock. The details of the shock fitting formulas and numerical methods can be found in (Zhong 1998).

III. FLOW CONDITIONS

The flow conditions for the test case studied in this paper are the same as those of Stetson *et al.*'s (1984) experiments on air flow over a blunt cone. The specific flow conditions are:

$M_\infty = 7.99$, $Re_{r_n} = \rho_\infty^* U_\infty^* r_n^* / \mu_\infty^* = 33,449$
$p_t^* = 4 \times 10^6\ Pa$, $T_t^* = 750\ K$
$\gamma = 1.4$, $Pr = 0.72$, $R^* = 286.94\ Nm/kgK$
Free-stream unit Reynolds number: $Re_\infty^* = 8.78 \times 10^6\ m^{-1}$
Blunt cone half angle: $\theta = 7^\circ$, zero flow angle of attack.
Parameters in Sutherland's viscosity law: $T_r^* = 288\ K$, $T_s^* = 110.33\ K$,
$\mu_r^* = 0.17894 \times 10^{-4}\ kg/ms$,

where p_t^* and T_t^* are total pressure and total temperature respectively. The body surface is a no-slip and adiabatic wall for the steady base flow solution.

As stated earlier in this paper, three cases of different nose radii are considered. The nose radii are the same as those considered in Rosenboom et al. (1999), i.e.,

Case A: $r_n^* = 3.81 \times 10^{-3}\ m$
Case B: $r_n^* = 1.778 \times 10^{-2}\ m$
Case C: $r_n^* = 4.2672 \times 10^{-2}\ m$

Meanwhile, all other parameters, such as freestream flow conditions, cone half angle, and surface boundary conditions, are the same for these three cases.

IV. FREE-STREAM FORCING WAVES

Free-stream acoustic disturbances are imposed in freestream to start the receptivity simulation. The free-stream perturbations of an arbitrary flow variable can be written in the following form:

$$q_\infty(x,y,t)' \quad = \quad |q'| \sum_{n=1}^{15} A_n \, e^{i[n\ \omega_1(\frac{x}{c_\infty}-t)+\phi_n]} \tag{2}$$

where c_∞ is the phase velocity in the free stream, and q represents any of the flow variables. In the equations above, $|q'|A_n$ is the free-stream wave amplitude of a given flow variable q at the n-th frequency of

$$\omega_n \quad = \quad n\ w_1 \qquad\qquad (n = 1, 2, \cdots, 15) \tag{3}$$

where w_1 is the minimum frequency of the wave packet. The minimum frequency ω_1 is chosen such that the frequencies span the dominant second-mode frequencies calculated by LST. Since the wave components of different frequencies are linearly independent, the initial phase angles, ϕ_n, of the forcing acoustic wave at frequency ω_n are chosen randomly. The forcing frequencies can also be represented by a dimensionless frequency F_n defined by

$$F_n \quad = \quad 10^6 \ \frac{\omega_n^* \nu^*}{U_\infty^{*2}}. \tag{4}$$

For fast acoustic waves in the free stream, perturbation amplitudes of nondimensional flow variables satisfy the following dispersion relations:

$$|\rho'|_\infty \quad = \quad |p'|_\infty/\gamma \ = \ |u'|_\infty M_\infty \ = \ \epsilon M_\infty \tag{5}$$

$$|s'|_\infty \quad = \quad |v'|_\infty \ = \ 0 \tag{6}$$

where ϵ is a dimensionless number representing the total amplitude of the group of 15 free-stream fast acoustic waves. In this paper, only linear receptivity is considered by using a very small value of ϵ.

V. STEADY BASE FLOW SOLUTION

The steady base flow solution is obtained first by computing the flow without free-stream forcing waves. In Zhong and Ma (2003), the steady base flow solutions of Case A was compared with those of Esfahanian & Herbert (1991 & 1993) and the experimental results of Stetson *et al.* We will mainly present the comparison of the effects of the nose radius on the steady base flow solutions here.

Figures 1 and 2 compare the steady pressure and temperature distributions along the cone surface among the three cases of different nose radii. Figure 1 shows that, for all three cases, the maximum wall pressure is reached at the stagnation point. The surface pressure drops sharply as flow expands around the nose region. Because of the discontinuity in surface curvatures at the junction of the spherical nose and straight cone afterward, the flow experiences an over-expansion at the junction and goes through a recompression along the cone surface afterward. As a result, there is adverse pressure gradient along the surface locations after the junction. Further downstream, the surface pressure approaches a constant value. The size of the region of the pressure drop and increase is proportional to the nose radius r_n.

Figure 2 shows that the nose radius also affects the wall temperature distribution. The maximum steady adiabatic wall temperature is reached at the stagnation point. The temperature drops gradually as s increases along the surface. At larger r_n, the wall temperature drops off at a much slower rate than that of smaller r_n.

The distributions of Mach number at locations immediately behind the bow shock are shown in Fig. 3. The flow is subsonic in the stagnation region. The Mach number increases to a constant as s increases. At larger r_n, the Mach number grows at a slower rate.

The main effect of the nose bluntness is the reduction of local Reynolds numbers in the mean flow due the existence of the entropy layer. Figures 4 to 6 show the Mach number contours for the three cases of different r_n with the same dimensional length in the x direction. In Case A of smallest r_n, the bow shock is very close to the cone surface. The boundary layer is very thin. On the other hand, for Case C of larger nose bluntness, the shock standoff distance is much larger. At the same time, the boundary layer is much thicker. This is an indication that the local Reynolds numbers of Case C are much lower than those of Case A.

The effect of nose bluntness on the steady base flow is shown in the tangential velocity profiles across the boundary layers at a fixed surface location of $s^* = 1.035m$, as shown in Fig. 7. The figure shows that the velocity of Case A has a thin boundary layer near the surface. On the other hand, Case B and C have much thicker boundary layers. The velocities of Case C are lower than those of Case A. Figure 8 shows similar profiles of temperatures across the boundary layer at the same $s^* = 1.035m$ location. Again, the entropy layer for cases of larger r_n results in much thicker boundary layers.

The entropy layer can be characterized by by means of a parameter, $\rho\frac{du_t}{dy_n}$. Figure 9 plots the $\rho\frac{du_t}{dy_n}$ profiles at the surface location of $s^* = 1.035m$. Again, at this surface station, Cases A of smallest r_n shows very little effect of entropy layer, while the profile of Case C is substantially different due to the influence of the entropy layer.

VI. Linear Stability Characteristics for Case A

The linear stability analysis has been done for Case A by many authors, as well as by Zhong and Ma (2003). The linear stability properties for Case B and Case C have been reported by Rosenboom et al. (1999). In addition, the results of a linear stability analysis can be used to identify the main components of boundary-layer disturbances from the results of numerical simulations of receptivity. In LST, a local Reynolds number, R, based on the length scale of the boundary-layer thickness is used:

$$R = \frac{\rho^*_\infty u^*_\infty L^*}{\mu^*_\infty}, \tag{7}$$

where L^* is the length scale of the boundary-layer thickness defined as

$$L^* = \sqrt{\frac{\mu^*_\infty s^*}{\rho^*_\infty u^*_\infty}}, \tag{8}$$

where s^* is the natural surface coordinate defined as the curve length along the wall surface measuring from the nose.

The LST is based on the normal mode analysis under a local parallel flow assumption. Specifically, the linear fluctuations of flow variables are decomposed into the following normal mode form:

$$q' = \hat{q}(y_n)\, e^{i\,(-\omega t + \alpha\, s)}, \tag{9}$$

where $\hat{q}(y_n)$ is the complex amplitudes of the disturbances, n and s are the local natural coordinates along the wall-normal and surface directions respectively, $\alpha = \alpha_r + i\alpha_i$, is the streamwise complex wave number. The variable q stands for any of the independent flow variables. In a spatial linear stability analysis, for a given real frequency ω, complex parameter α and complex function $\hat{q}(y)$ are obtained as an eigenvalue and eigenfunction of the stability equations. The real and imaginary parts of α, α_r and α_i, represent the spatial wave number and growth rate of a wave mode respectively. A linear wave mode is unstable when α_i is negative. The real part of the wave number α_r is related to phase velocity of a wave mode by

$$a = \frac{\omega}{\alpha_r} = \frac{10^{-6} FR}{\alpha_r}, \tag{10}$$

where a is the nondimensional phase velocity normalized by the free-stream velocity.

Figure 10 shows the distributions of the phase velocities (Eq. (10)) of three discrete modes, mode I, mode II and the Mack modes (including the first and the second modes), as functions of frequencies at $s = 175$ $(0.667m)$ for Case A. The phase velocities of the fast acoustic wave $(1 + 1/M_\infty)$, entropy/vorticity wave (1), and slow acoustic wave $(1 - 1/M_\infty)$ are also shown in the figure for comparison. Both mode I and mode II originate from the fast acoustic wave with an initial phase velocity of $1 + 1/M_\infty$. Before these two modes become distinct modes, their eigenvalues merge with the fast acoustic spectrum branch. After these two wave modes appear as discrete modes, their phase velocities decrease gradually with increasing ω. As a result, the phase-velocity differences between mode I (or mode II) and the fast acoustic waves become larger as ω increases. On the other hand, the first mode originates from the slow acoustic wave side with an initial phase velocity close to $1 - 1/M_\infty$. Furthermore, the phase velocity curve of the first mode shows an opposite trend when ω increases. As ω increases, the phase velocity of the first mode increases and intersects with phase velocity curve of mode I at the location with $\omega = 0.1825$. After passing the intersection point, the first mode convert to the second mode. As it was shown in our previous study (Ma and Zhong 2003a), the first mode and the second mode identified by Mack are in fact different sections of a single wave mode, which is confirmed in in phase velocity curve shown in Fig. 10 and growth rate curve shown in Fig. 11. Therefore, both the first and the second Mack mode are simply called Mack modes in order to be consistent with Mack's generally accepted terminology. In the vicinity of the intersection point between mode I and the first mode, the phase velocity of the first mode drops a little, and phase velocity of the Mack modes increases again after it clearly becomes the second mode. Similarly, Mode II eventually intersect with the Mack mode at a high frequency.

In the receptivity study, we are more interested in the resonant interaction between mode I and the firs mode. At the intersection point between mode I and the first mode ($\omega = 0.1825$ for $s = 175$), mode I is synchronized with the Mack mode because the two modes have the same frequency, phase velocity and wave number. Therefore, there is a resonant interaction between mode I and the Mack mode near this intersection location. In addition, both modes have very similar profiles of perturbation eigenfunctions across the boundary layer at this location. The only exception is that the two modes have different growth rates (α_i). Here, the growth rates of the Mack modes at the same station for Case A are compared with those of other boundary-layer normal modes in Fig. 11. While the growth rates of the Mack modes are continuous, there are gaps in the growth rate curves for mode I and mode II. The figure shows that both mode I and mode II are always stable. When they initially appear at relatively low frequency, these two modes are close to neutrally stable with zero growth rates. As ω increases, their growth rates are always on the stable side and rapidly become more stable. On the other hand, the Mack modes are unstable in multiple regions of different frequencies. The Mack modes are slightly unstable in the range of ω between 0.0485 and 0.126 $(33.1kHz < f^* < 86.1kHz)$. The Mack mode in this range is the conventional first mode identified by Mack (1984). In the range of ω between 0.171 and 0.243 $(116.7kHz < f^* < 165.9kHz)$, the unstable Mack modes are the conventional second mode identified by Mack. In this range, the growth rates of the second mode increases to a peak and decays afterward. The second Mack mode has the largest growth rate at $\omega = 0.198$ $(f^* = 135kHz), s = 175$ $(0.667m)$.

Another important characteristic of boundary-layer instability modes is the neutral stability curve for frequencies versus Reynolds numbers. The current results on neutral stability curve for Case A are compared with that of Malik (1990) in Fig. 12. Dimensional frequencies f^* are used in the figure because the experimental results were presented using dimensional frequencies. The dimensional frequencies can be converted easily to dimensionless frequencies F by using Eq. (4). The synchronization locations between mode I and the Mack modes are also plotted in the same figure because the synchronization locations between mode I and the Mack modes play an important role in the receptivity process (Ma & Zhong 2002, 2003a, 2003b). There are two peaks in the neutral stability curve. The first peak with lower frequencies (lower than 100 kHz) is for the first Mack mode instability, while the second peak with higher frequencies (higher than 100 kHz) is for the second mode instability. Based on the current results, the critical local Reynolds number (R) for the onset of the boundary-layer instability is the second mode instability at the surface

location of 1580, which corresponds to $s = 75$ $(0.286m)$ and $x = 72.5$ $(0.276m)$. This critical value is very close to Malik's result $R = 1540$ for $s = 70.9$ $(0.270m)$ and $x = 68.8$ $(0.262m)$. Below this critical Reynolds number, all boundary-layer wave modes are stable. The first unstable two-dimensional first mode appear at $R = 2270$, which corresponds to the $s = 154$ $(0.587m)$surface station. Figure 12 also shows that both the first and the second modes are stable when frequencies are higher than 180 Khz.

VII. RECEPTIVITY TO FREE-STREAM NOISE

The receptivity to free-stream fast acoustic waves for the three cases is studied by numerical simulation. The free-stream forcing waves are a mixture of 15 independent planar fast acoustic waves of different frequencies, i.e.,

$$f_n^* = n\, f_1^* \qquad (n = 1, 2, \cdots, N; N = 15) \tag{11}$$

where the lowest frequencies are $f_1^* = 14.92kHz$ (Case A), $5.799kHz$ (Case B), and $3.323kHz$ (Case C), respectively. As shown in Rosenboom et al.'s LST results, the most unstable frequencies for the first and second modes decrease when r_n increases. The frequency range used in the current simulation for the three cases are chosen in order to cover the most unstable frequencies according to Rosenboom et al.'s LST results.

The relative wave amplitudes among different frequencies in the free stream are set to be the same. The phase angles of the free-stream forcing waves of the 15 frequencies given by Eq. (2) are chosen randomly. The 15 sets of wave frequencies used in the three cases of receptivity simulation are listed in Table 1. The overall free-stream wave amplitude used in the simulation is $\epsilon = 1.0 \times 10^{-4}$, which is small enough that the receptivity process falls in the linear regime.

Table 1. Forcing acoustic wave components of 15 frequencies in the free stream for Case A, B, and C.

Case A ($r_n^* = 3.81\,mm$)			**Case B** ($r_n^* = 17.78\,mm$)			**Case C** ($r_n^* = 42.672\,mm$)		
n	f_n^* (kHz)	F_n	n	f_n^* (kHz)	F_n	n	f_n^* (kHz)	F_n
1	14.92	9.035	1	5.799	3.512	1	3.323	2.012
2	29.84	18.07	2	11.60	7.023	2	6.646	4.024
3	44.77	27.11	3	17.40	10.53	3	9.969	6.036
4	59.68	36.14	4	23.20	14.05	4	13.29	8.049
5	74.61	45.18	5	29.00	17.56	5	16.62	10.06
6	84.53	54.21	6	34.80	21.07	6	19.94	12.07
7	104.5	63.25	7	40.60	24.58	7	23.26	14.08
8	119.4	72.28	8	46.40	28.09	8	26.58	16.10
9	134.3	81.31	9	52.19	31.60	9	29.91	18.11
10	149.2	90.35	10	57.99	35.12	10	33.23	20.12
11	164.1	99.39	11	63.79	38.63	11	36.55	22.13
12	179.1	108.4	12	69.59	42.14	12	39.87	24.15
13	194.0	117.5	13	75.39	45.65	13	43.20	26.16
14	208.9	126.5	14	81.19	49.16	14	46.52	28.17
15	223.8	135.5	15	86.99	52.67	15	49.85	30.18

The unsteady calculations are carried out until the solutions reach a periodic state in time. Temporal Fourier analysis is then carried out on the local perturbations of unsteady flow variables. A Fourier transform

for the perturbation field of an arbitrary flow variable q leads to:

$$q'(x,y,t) = \Re\{\sum_{n=0}^{N} |q_n(x,y)|\ e^{i\,[-n\omega_1 t + \phi_n(x,y)]}\}\ , \tag{12}$$

where $n\omega_1$ is the frequency of the n-th wave mode, $q'(x,y,t)$ represents an arbitrary perturbation variable. The Fourier transformed variables, $|q_n(x,y)|$ and $\phi_n(x,y)$, are spatially varying real variables representing the local perturbation amplitudes and phase angles at the wave frequency of $n\omega_1$.

Case A ($r_n^* = 3.81 \times 10^{-3}\ m$)

Figure 13 shows the distributions of amplitudes of the pressure perturbations, $|p_n(x,y)|$, for the 15 forcing frequencies along the cone surface for Case A. The dimensionless x coordinates are nondimensionalized by the nose radius of $r_n^* = 3.81 \times 10^{-3}\ m$. Each line in these figures represents one of the 15 frequencies given by Eq. (11). These figures show that the receptivity process leads to complex induced wave structures in the boundary layer. The wave structures are different for different frequencies. For perturbations at a fixed frequency, the disturbance wave structures are also different at different sections of the cone surface. The figure shows that there is strong amplitude growth near the exit of current computational domain for the three frequencies of $n = 7, 8, 9$ although there is oscillation in amplitudes caused by modulation between different waves.

In (Zhong and Ma 2003), the results of the LST were used to identify different dominant wave modes induced in the boundary layer by the free-stream fast acoustic waves. For the development of wave components at a relatively low frequency of 74.61 kHz ($n = 5$ and $F = 45.2$), the amplitudes of the induced pressure disturbances in the boundary layer increase initially until reaching a peak located approximately at the station of $x = 109.2$ ($0.416m$). After a decay between the stations of $x = 109.2$ and $x = 200$ ($0.762m$), the disturbances at this frequency begin to grow and decay again. It was shown that mode I waves, other than the Mack mode waves, are generated inside the boundary layer at this frequency. This is a natural consequence of the fact that mode I waves are synchronized with the forcing fast acoustic waves in the nose region. The wave synchronization results in resonant interaction between mode I and the forcing acoustic waves, which leads to generation and amplification of mode I waves in the boundary layer.

On the other hand, for a higher frequency of 119.4 kHz ($n = 8$ and $F = 72.3$), Fig. 13 shows that the amplitudes of the induced disturbances in the boundary layer increase initially, reach a peak approximately at the surface station of 30 nose radii ($0.114m$), and decay afterward. In the following region between the surface station of 65 nose radii (0.248) to approximately 190 nose radii (0.724), the amplitudes of the disturbance waves stay at an approximately constant level with slight fluctuations. The wave amplitudes increase dramatically in the region downstream of the surface station at $s = 192$ ($0.732m$). It was shown in (Zhong and Ma 2003) that mode I waves are generated by their resonant interactions with the forcing fast acoustic waves near the nose. In the downstream region of $x > 200$ ($0.762m$), the boundary-layer disturbances at the frequency of $n = 8$ are strongly amplified. The induced perturbations at this frequency in the boundary layer are dominantly the unstable second Mack mode at this surface location. It was shown by Zhong and Ma (2003) that the second mode is generated by its resonant interactions with the mode I waves, which in turn are generated by the forcing fast acoustic waves in the nose region through separate resonant interactions. The resonant interaction mechanism also explains the fact that the second Mack mode is not generated in the boundary layer before the synchronization point between mode I and the second mode ($x = 192$, $0.731m$), even though the second Mack mode becomes unstable at the earlier surface stations of the 143.4 nose radii ($0.546m$).

Case B ($r_n^* = 1.778 \times 10^{-2}\ m$)

Figures 14 to 17 show the distributions of amplitudes of the pressure perturbations, $|p_n(x,y)|$, for the 15 forcing frequencies along the cone surface for Case B.

Figures 14 and 15 show the amplitude development along the cone surface for the first group of seven lowest frequencies, ranging from 4.80 kHz to 40.6 kHz ($n = 1, \cdots, 7$ in Table 1). The figures show that the amplitude distributions are relatively smooth, which is an indication that the perturbations are dominated by a single wave mode. The induced waves demonstrate growth in amplitudes. For example, for the frequency of $n = 3$ $(17.4kHz)$, the wave amplitudes start to grow at $s^* = 0.2m$. The amplitudes reach a peak at $s^* = 4.4m$, and start to decay afterward. As the frequency increases, the length of growth region is reduced. The growth patterns at these frequencies for Case B are same as those of $n = 5$ $(74.61kHz)$ for Case A (Fig. 13). As demonstrated in (Zhong and Ma 2003), this amplitude growth is a results of the resonant interaction between the forcing acoustic waves and the stable mode I wave. The maximum growth in amplitudes are relatively small compared to the second Mack mode growth at higher frequencies.

Figure 16 shows the amplitude development along the cone surface for the next group of two frequencies at $n = 8, 9$ (Table 2). The two frequencies are 46.4 kHz and 52.2 kHz respectively. There is a strong amplitude growth near the exit of current computational domain for these two frequencies, although there are oscillations in amplitudes caused by modulation between different waves. Again, this wave pattern is the same as the second mode growth pattern for Case A. As shown in (Zhong and Ma 2003), the growth of the second mode is a result of a two step receptivity mechanisms. The forcing acoustic waves excite mode I wave near the nose region. The induced mode I in turn excite the second Mack mode by resonant interaction at a downstream location. For the frequency of $n = 8$ for Case B, the second mode begins to grow at approximately $x^* = 5m$, while the second mode starts to grow when $x^* > 4m$ for $n = 9$. On the other hand, for $n = 9$ of Case A of smaller r_n, the second mode starts to grow when $x^* = 200 * r_n = 0.762m$, which much upstream of the instability locations for Case B. Therefore, the increase of r_n leads to a significant downstream shift of the onset location of the second mode in the receptivity process. This finding is consistent with the LST results of Rosenboom et al. (1999).

Figure 17 shows that there are very strong oscillations in amplitude development along the cone surface for three highest frequencies with $n = 10, 11, 12$. There is no second mode excitation at these high frequencies.

Case C $(r_n^* = 4.2672 \times 10^{-2}\, m)$

Figures 18 to 20 show the distributions of amplitudes of the pressure perturbations, $|p_n(x, y)|$, for the 15 forcing frequencies along the cone surface for Case C. These figures show that the amplitude growth starts in the region near the nose. The locations of initial amplitude growth are not sensitive to the change in frequency. The amplitude reaches a peak at a downstream location and then decays afterward.

For example, for the frequency of $n = 5$ $(16.6kHz)$, the wave amplitudes start to grow at $s^* = 0.2m$. The amplitude growth reaches a peak at $s^* = 3m$. As the frequency increases, the length of growth region is reduced. Again, the growth properties at these frequencies for Case C are the same as the mode I growth for Case A. As demonstrated in (Zhong and Ma 2003), this growth is a results of the resonant interaction between the forcing acoustic waves and the stable mode I wave. The maximum growth in amplitudes are small compared to the second Mack mode growth at higher frequencies. The figures also show that after the decay of mode I waves, there are strong modulation of waves in the results. The second mode instability cannot be observed in the results because the total length of the computational domain is not longer enough for Case C. It is expected that the second mode instability will be excited at surface location still further downstream, if the receptivity simulation was carried out to further downstream. Again, the increase in r_n results in significant delay in the onset of the second mode excitation in the receptivity process. No reversal in the onset of instability induced by the receptivity process can be observed in the simulation results of the three cases considered in this paper.

VIII. CONCLUSIONS

The effect of nose bluntness on the receptivity of Mach 7.99 flow over a 7° half-angle blunt cone, corresponding to Stetson *et al.*'s boundary-layer stability experiments, has been studied by numerical simulation.

Three cases of different nose radii, including both "small" and "large" bluntness, have been considered.

The steady flow solutions of the full Navier-Stokes equations show that the nose bluntness leads to a thicker boundary layer near the nose region. In addition, the region influenced by the entropy layer becomes longer as the noise radius increases.

The receptivity to free-stream fast acoustic waves is subsequently investigated by numerical simulation. It is found that the basic receptivity mechanisms of the current axisymmetric hypersonic flow over a blunt cone with three nose radii are essentially the same. Specifically, the receptivity is caused by the resonant interaction between the forcing waves and a boundary-layer wave mode (mode I) near the leading edge, and the resonant interaction between the induced stable boundary-layer wave mode (mode I) and the secodn Mack mode in a downstream location. When the nose radius is increased, the location of the initial excitation of the second instability mode always moves downstream. No instability reversal is observed as the nose radius is increased. In order to understand the cause of transition reversal phenomenon, further studies are necessary to investigate the nose bluntness effects under other factors, including receptivity to the different forcing waves, surface roughness, larger nose bluntness, three-dimensional waves, and nonlinear interaction.

IX. ACKNOWLEDGMENTS

This work was sponsored by the Air Force Office of Scientific Research, USAF, under AFOSR Grant #FA9550-04-1-0029, monitored by Dr. John Schmisseur. The views and conclusions contained herein are those of the authors and should not be interpreted as necessarily representing the official policies or endorsements either expressed or implied, of the Air Force Office of Scientific Research or the U.S. Government.

References

[1]A. Demetriades. 1974 Hypersonic Viscous Flow Over A Slander Cone. Part III: Laminar Instability and Transition. *AIAA paper 74-535.*

[2]A. Demetriades. 1977 Laminar Boundary Layer Stability Measurements at Mach 7 Including Wall Temperature Effects. *AFOSR-TR-77-1311.*

[3]L. E. Ericsson 1987 Effects of Nose Bluntness and Cone Angle on Slender Vehicle Transition. *AIAA Paper 87-1415.*

[4]V. Esfahanian. 1991 *Computation and stability analysis of laminar flow over a blunt cone in hypersonic flow.* PhD thesis, The Ohio State University.

[5]A. V. Fedorov and A. Tumin. 2001 Initial-Value Problem for Hypersonic Boundary Layer Flows. *AIAA Paper 2001-2781.*

[6]Alexander V. Fedorov and Andrew P. Khokhlov. 2001 Prehistory of Instability in a Hypersonic Boundary Layer. *Theoretical and Computational Fluid Dynamics*, 14:359–375,

[7]A. V. Fedorov. 2002 Receptivity of High Speed Boundary Layer to Acoustic Disturbances. *AIAA Paper 2002-2846.*

[8]A. V. Fedorov and A. P. Khokhlov. 2002 Receptivity of Hypersonic Boundary Layer to Wall Disturbances. *Theoretical and Computational Fluid Dynamics*, 15:231–254.

[9]A. V. Fedorov 2003 Receptivity of a high-speed boundary layer to acoustic disturbances . *Journal of Fluid Mechanics*, 491:101 -129.

[10]Th. Herbert and V. Esfahanian. 1993 Stability of Hypersonic Flow over a Blunt Body. *AGARD CP-514*, pp. 28-1 – 12.

[11]E. Kufner and U. Dallmann. 1994 Entropy- and Boundary Layer Instability of Hypersonic Cone Flows – Effects of Mean Flow Variations. *IUTAM Symposium on Laminar-Turbulent Transition*, Sendai/Japan, September 1994, pp. 197-204, Springer-Verlag, Berlin.

[12]E. Kufner, U. Dallmann, and J. Stilla. 1993 Instability of Hypersonic Flow Past Blunt Cones – Effects of Mean Flow Variations. *AIAA paper 93-2983.*

[13]Y. Ma and X. Zhong. 2001 Numerical Simulation of Receptivity and Stability of Nonequilibrium Reacting Hypersonic Boundary Layers. *AIAA paper 2001-0892.*

[14]Y. Ma and X. Zhong. 2002 Receptivity to Free-stream Disturbances of Mach 4.5 Flow over A Flat Plate. *AIAA Paper 2002-0140.*

[15]Y. Ma and X. Zhong. 2003a Receptivity of a supersonic boundary layer over a flat plate. Part 1: wave structures and interactions. *Journal of Fluid Mechanics*, 488:31-78.

[16]Y. Ma and X. Zhong. 2003b Receptivity of a supersonic boundary layer over a flat plate. Part 2: receptivity to free-stream sound,. *Journal of Fluid Mechanics*, 488:79-121.

[17]Y. Ma and X. Zhong. 2003c Receptivity to Free-stream Disturbances of Mach 8 Flow over a Sharp Wedge. *AIAA paper 2003-0788.*

[18]M. R. Malik. 1990 Numerical methods for hypersonic boundary layer stability. *Journal of Comp. Phys.*, 86:376–413.

[19]M. R. Malik, R. E. Spall, and C.-L. Chang. 1990 Effect of Nose Bluntness on Boundary Layer Stability and Transition. *AIAA paper 90-0112.*

[20]A. A. Maslov, S. G. Mironov, and A. A. Shiplyuk. 2002 Hypersonic Flow Stability Experiments. *AIAA Paper 2002-0153.*

[21]A. A. Maslov, A. N. Shiplyuk, A. Sidorenko, and D. Arnal. 2001 Leading-edge receptivity of a hypersonic boundary layer on a flat plate. *Journal of Fluid Mechanics*, 426:73–94.

[22]J. L. Potter and J. D. Whitfield. 1962 Effects of Slight Nose Bluntness and Roughness on Boundary-Layer Transition in Supersonic Flows. *Journal of Fluid Mechanics*, Vol. 12, part 4, pp. 501–535.

[23]I. Rosenboom and S. Hein and U. Dallmann 1999 Influence of Nose Bluntness on Boundary-Layer Instabilities in Hypersonic Cone Flows *AIAA Paper 99-3591.*

[24]K. F. Stetson and R. Kimmel. 1993 On the Breakdown of a Hypersonic Laminar Boundary Layer. *AIAA Paper 93-0896.*

[25]K. F. Stetson and R. L. Kimmel. 1992. On Hypersonic Boundary Layer Stability. *AIAA paper 92-0737.*

[26]K. F. Stetson, E. R. Thompson, J. C. Donaldson, and L. G. Siler. 1984 Laminar Boundary Layer Stability Experiments on a Cone at Mach 8, Part 2: Blunt Cone. *AIAA paper 84-0006.*

[27]X. Zhong. 1997a Direct Numerical Simulation of Hypersonic Boundary-Layer Transition Over Blunt Leading Edges, Part II: Receptivity to Sound (Invited). *AIAA paper 97-0756.*

[28]X. Zhong. 1997b Direct Numerical Simulation of Hypersonic Boundary-Layer Transition Over Blunt Leading Edges, Part I: New Numerical Methods and Validation (Invited). *AIAA paper 97-0755, 35th AIAA Aerospace Sciences Meeting and Exhibit, January 6-9, Reno, Nevada.*

[29]X. Zhong. 1998 High-Order Finite-Difference Schemes for Numerical Simulation of Hypersonic Boundary-Layer Transition. *Journal of Computational Physics*, 144:662–709.

[30]X. Zhong. 2001 Leading-Edge Receptivity to Free Stream Disturbance Waves for Hypersonic Flow Over A Parabola. *Journal of Fluid Mechanics*, 441:315–367.

[31]X. Zhong and M. Tatineni. 2001 Stable High-Order Schemes and DNS of Boundary-Layer Stability on a Blunt Cone at Mach 8. *AIAA Paper 2001-0437.*

[32]X. Zhong and Y. Ma 2004 Numerical Simulation of Leading Edge Receptivity of Stetson's Mach 8 Blunt Cone Stability Experiments. *AIAA Paper 2003-1133.*

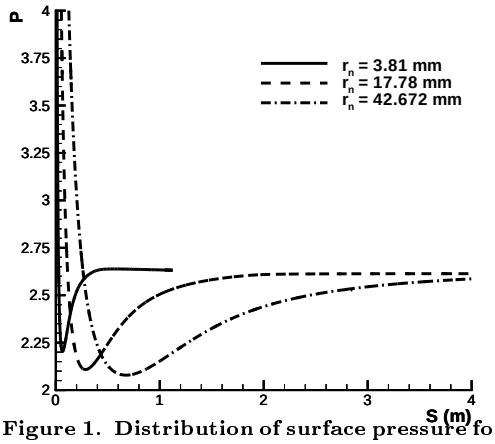

Figure 1. Distribution of surface pressure for the three cases of different nose radii for steady Mach 7.99 flow over a 7° half-angle blunt cone.

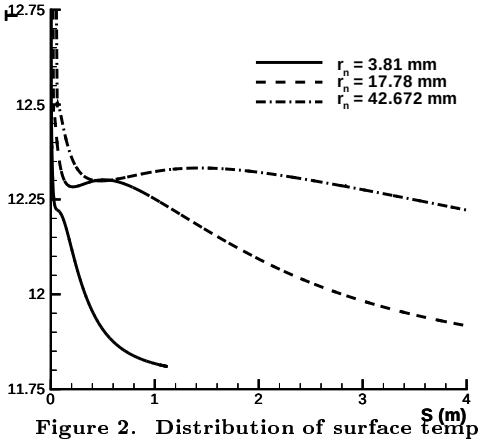

Figure 2. Distribution of surface temperature.

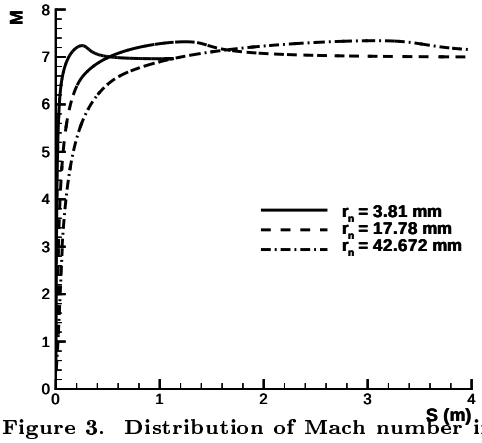

Figure 3. Distribution of Mach number immediately behind the bow shock.

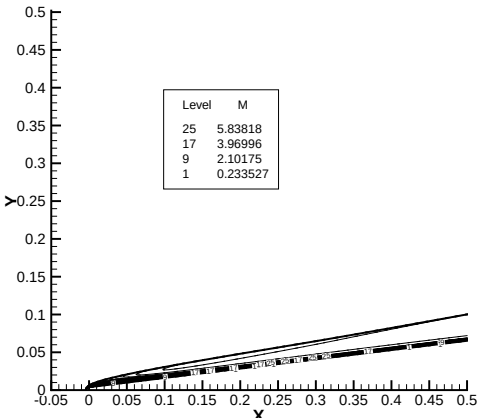

Figure 4. Contours of Mach number for Case A of $r_n^* = 3.81 \times 10^{-3}\ m$.

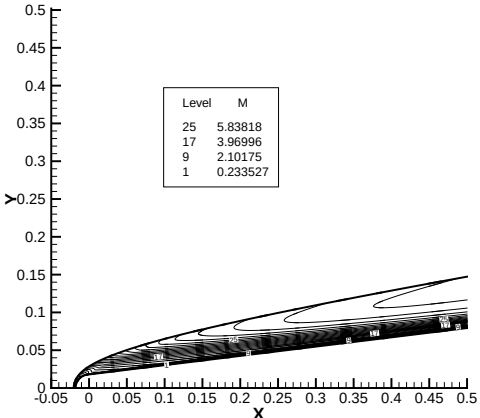

Figure 5. Contours of Mach number for Case B of $r_n^* = 1.778 \times 10^{-2}\ m$.

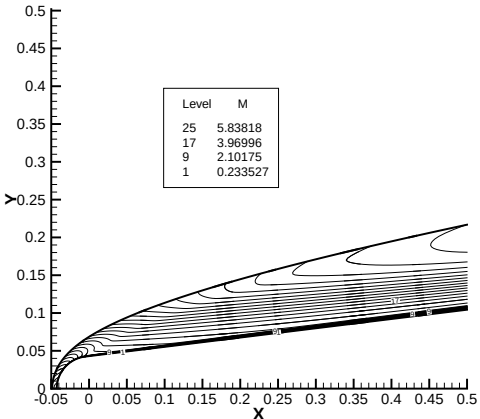

Figure 6. Contours of Mach number for Case A of $r_n^* = 4.2672 \times 10^{-2}\ m$.

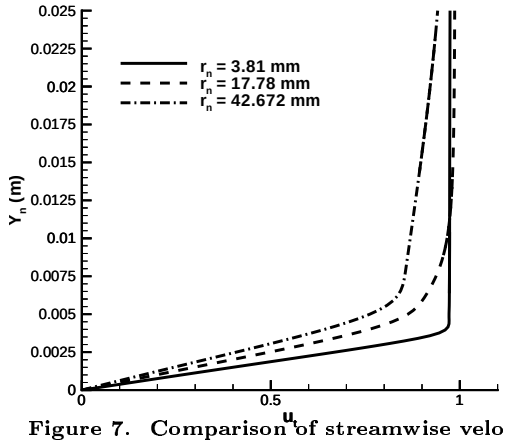

Figure 7. Comparison of streamwise velocity profiles among Cases A, B, and C at $s^* = 1.035m$.

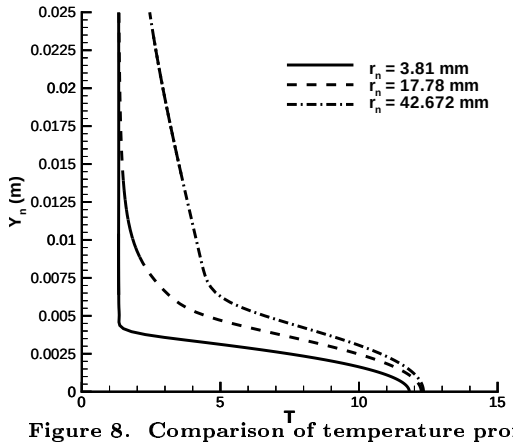

Figure 8. Comparison of temperature profiles among Cases A, B, and C at $s^* = 1.035m$.

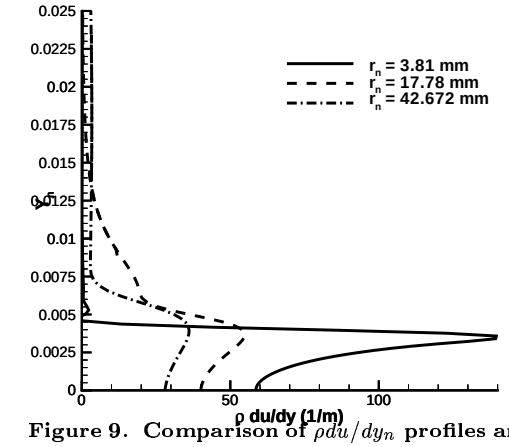

Figure 9. Comparison of $\rho du/dy_n$ profiles among Cases A, B, and C at $s^* = 1.035m$.

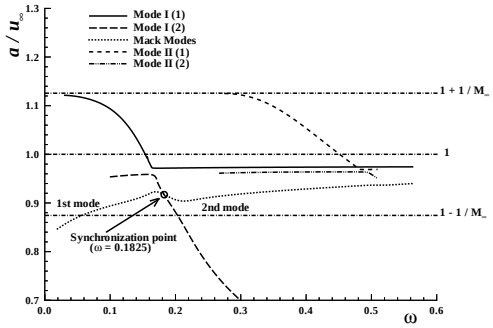

Figure 10. Distributions of the phase velocities of three discrete modes at $s^* = 175$ $(0.667m)$ for Case A.

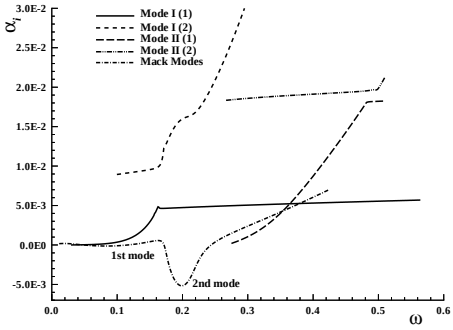

Figure 11. Distributions of the growth rates at the surface station of $s^* = 175$ $(0.667m)$ for Case A.

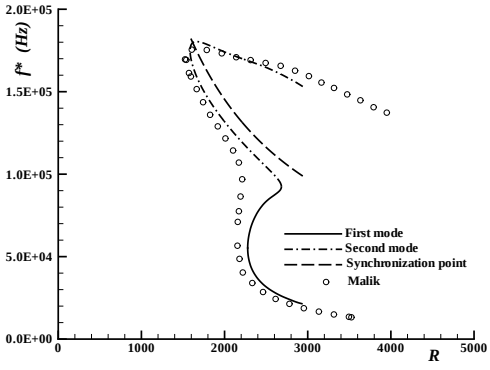

Figure 12. Comparison of the current neutral stability curve of the Mack modes with Malik's (1990) results for Case A.

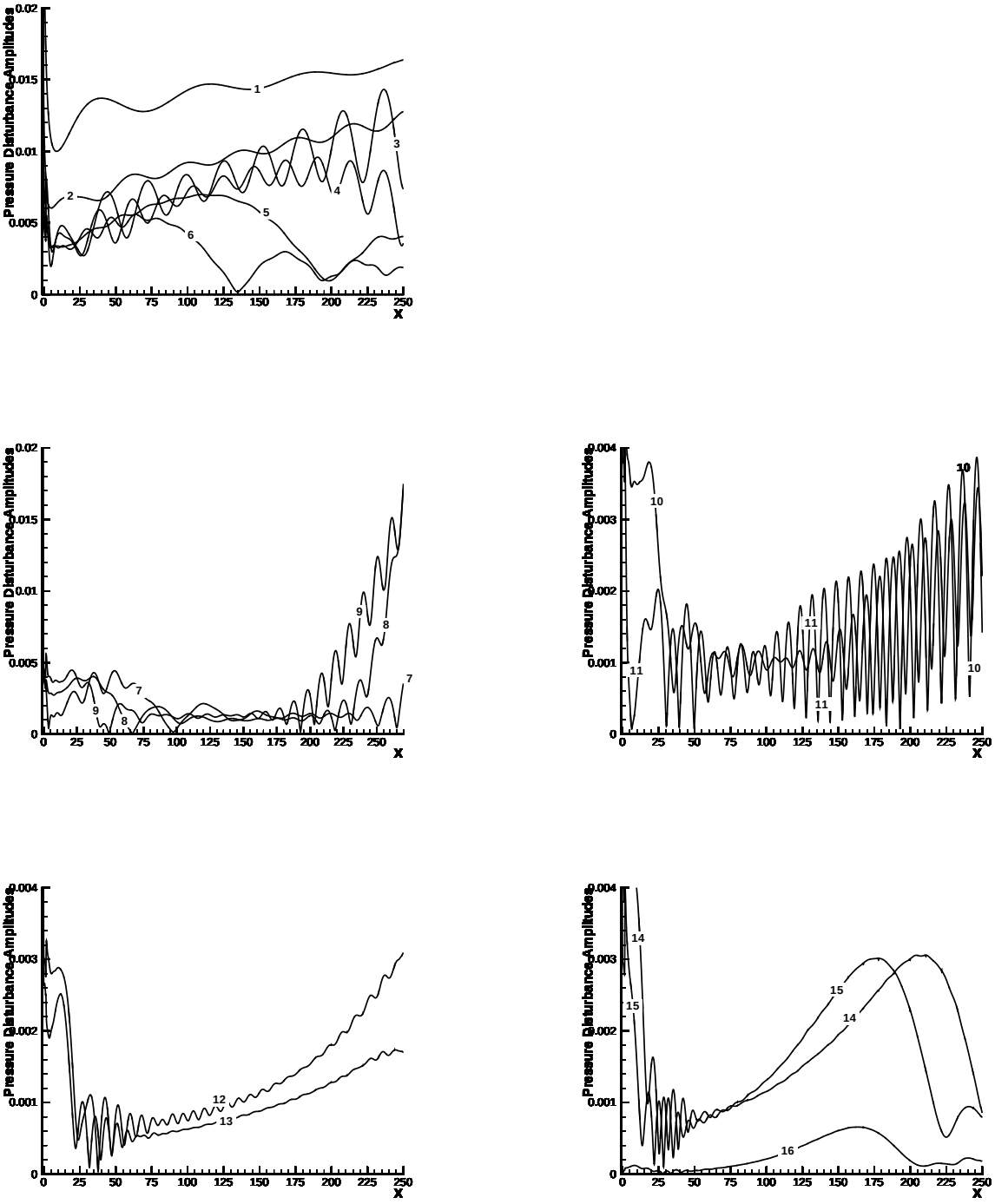

Figure 13. Amplitude distributions of the induced pressure perturbations along the cone surface for Case A (The lines represent 15 different frequencies of $f_n^* = nf_1^*$, where $f_1^* = 14.922kHz$, $x^* = x \times 0.00381m$).

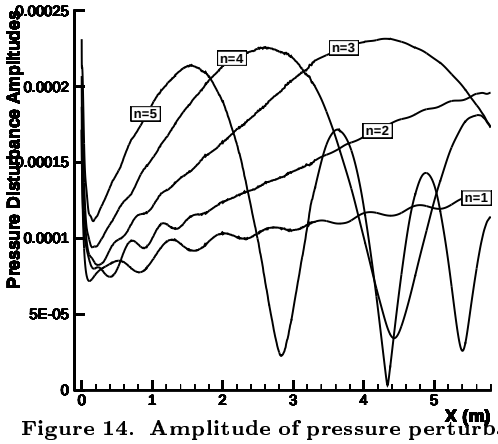

Figure 14. Amplitude of pressure perturbations along the cone surface for Case B ($f_n^* = nf_1^*$, where $f_1^* = 5.80kHz$).

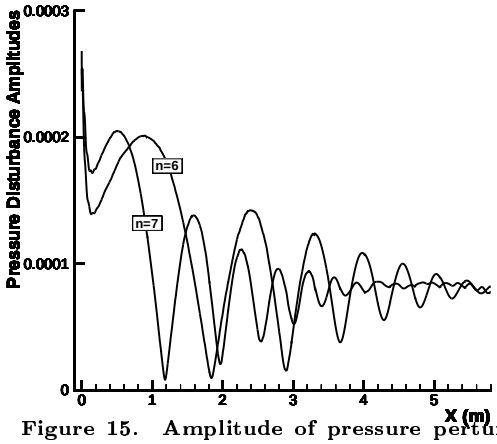

Figure 15. Amplitude of pressure perturbations for Case B ($f_n^* = nf_1^*$, where $f_1^* = 5.80kHz$).

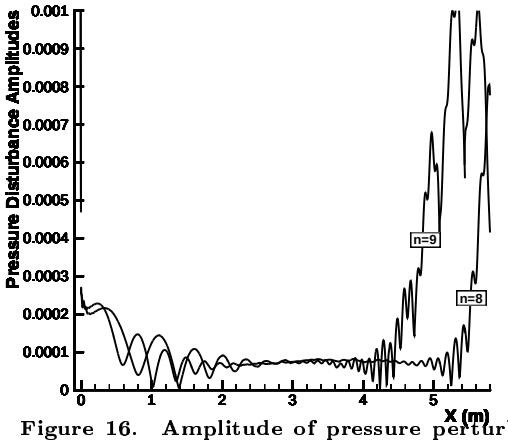

Figure 16. Amplitude of pressure perturbations for Case B ($f_n^* = nf_1^*$, where $f_1^* = 5.80kHz$).

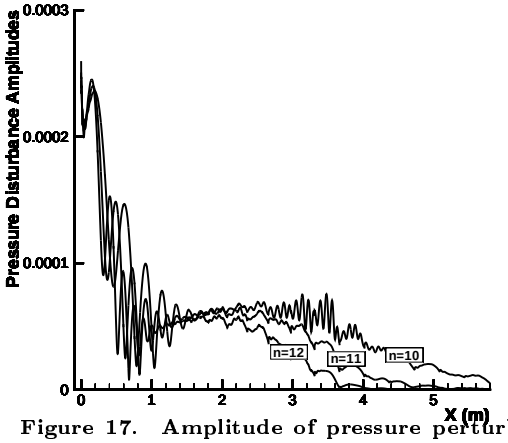

Figure 17. Amplitude of pressure perturbations for Case B ($f_n^* = nf_1^*$, where $f_1^* = 5.80kHz$).

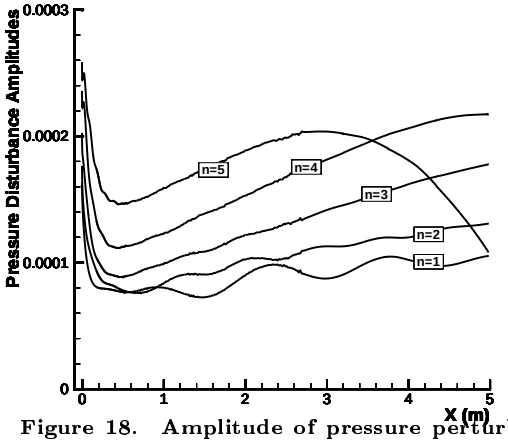

Figure 18. Amplitude of pressure perturbations for Case C ($f_n^* = nf_1^*$, where $f_1^* = 3.32kHz$).

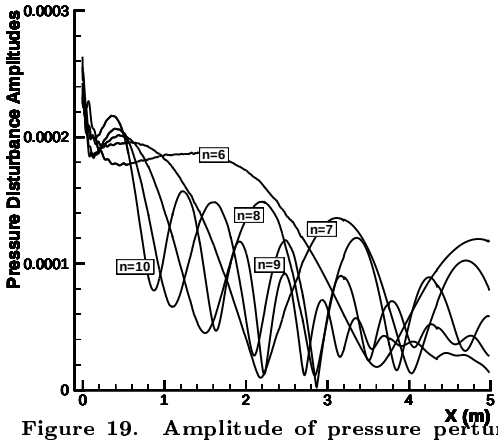

Figure 19. Amplitude of pressure perturbations for Case C ($f_n^* = nf_1^*$, where $f_1^* = 3.32kHz$).

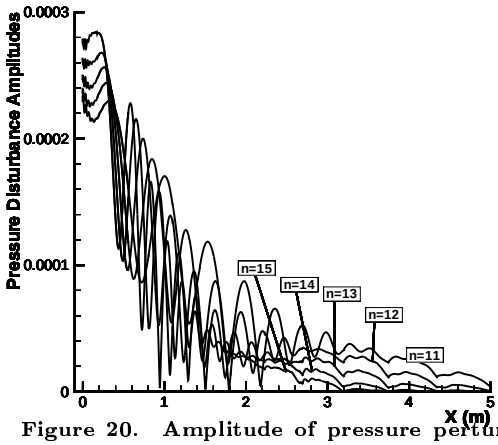

Figure 20. Amplitude of pressure perturbations for Case C ($f_n^* = nf_1^*$, where $f_1^* = 3.32kHz$).